Geophysical Journal International

Geophys. J. Int. (2012) **189,** 1475–1482 doi: 10.1111/j.1365-246X.2012.05437.x

Digital rock physics: numerical prediction of pressure-dependent ultrasonic velocities using micro-CT imaging

Claudio Madonna, Bjarne S. G. Almqvist and Erik H. Saenger

Geological Institute, ETH Zurich, 8092 *Zurich, Switzerland. E-mail: claudio.madonna@erdw.ethz.ch*

Accepted 2012 February 26. Received 2012 February 16; in original form 2011 August 12

SUMMARY

Digital rock physics combines modern microscopic imaging with advanced numerical simulations to analyse the physical properties of rocks. Elastic-wave propagation modelling based on the microstructure images is used to estimate the effective elastic properties of the rock. The goal of this paper is to describe and understand how laboratory experiments compare with digital rock physics results using Berea sandstone. We experimentally measure pressure-dependent ultrasonic velocities and the pore size distribution. The effective elastic properties resulting from numerical simulations are based on microcomputed tomography (micro-CT) images, which are systematically stiffer than the laboratory measures. Because the tomographic images do not resolve the small-scale pore and crack network of the sample, we hypothesize that the numerical overprediction is attributable to the smallest pores and grain-to-grain contacts that are missing in the images. To reconcile the difference between numerical and experimental data, we suggest to use a grain boundary reconstruction algorithm. This allows to implement and approximate so far unresolved features in the virtual rock model. As a result, we can predict pressure-dependent effective velocity using micro-CT images.

Key words: Microstructures; Wave propagation; Acoustic properties; Mechanics, theory, and modelling.

1 INTRODUCTION

Over the last decade, microtomography has rapidly evolved to become a common microscopy tool in the geosciences. Different kinds of tomograms can be obtained depending on the physical phenomena of the applied investigation techniques. In Fig. 1, the various advanced 3-D microscopy methods are schematically shown with respect to the volume, which can be analysed, together with the resolution of the respective methods. Digital rock physics combines modern microscopic imaging with advanced numerical simulations for analysis of the physical properties of rocks, complementing laboratory investigations. X-ray microcomputed tomography (micro-CT) is among the emerging techniques used for digital rock physics. It allows analysis of a representative volume with a resolution down to the nanometric range (Holzer & Cantoni 2011) in a non-destructive way and enables the reconstruction of a realistic virtual 3-D model of a porous material. Indeed, 3-D micro-CT imaging and subsequent numerical determination of petrophysical properties have been applied in several studies (Øren *et al.* 2007; Sakellariou *et al.* 2007; Dvorkin *et al.* 2008; Malinouskaya & Mourzenko 2008; Saenger *et al.* 2011). These techniques allow for calculation of transport properties (Arns *et al.* 2001; Keehm *et al.* 2004; Harting *et al.* 2005; Knackstedt & Arns 2005) and effective mechanical properties (Arns *et al.* 2002; Saenger *et al.* 2004; Madadi *et al.* 2009). Elastic-wave propagation modelling based on the microstructure images is used to estimate the effective elastic properties (Saenger 2008).

As with every microscopic imaging technique, there is a trade-off between the maximum resolution and the investigated volume (Fig. 1). Because a representative volume of a porous rock is imaged using the micro-CT technique, the smallest pores, microcracks and grain-to-grain contacts stay unresolved. Such microstructures may significantly influence the mechanical properties of a rock. For example, the elastic properties of granular material strongly depend on the grain-to-grain contacts (Leurer & Dvorkin 2006), which micro-CT imaging may not resolve.

The goal of this paper is to describe and understand how laboratory measurements of ultrasonic *P*-wave velocities compare with digital rock physics results based on the geometric microstructural details present in segmented micro-CT images. Using grain boundary reconstruction algorithms, we present a method for calibrating the numerically overestimated effective elastic properties using experimental data obtained from a sample of Berea sandstone. We also suggest a strategy to predict pressure-dependent velocity using micro-CT images. A workflow is delineated that identifies the grain-to-grain contacts in the micro-CT images and assigns to them, based on laboratory calibration, weaker micromechanical properties for the subsequent numerical modelling.

2 BEREA SANDSTONE CHARACTERIZATION

For the laboratory experiments, a sandstone sample from the Berea Sandstone™ Petroleum Cores (OH, USA) was used. To determine

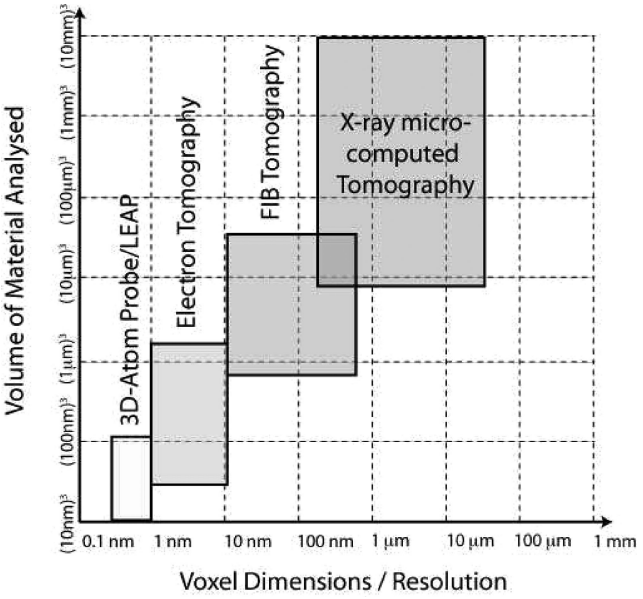

Figure 1. Comparison of X-ray microcomputed tomography (micro-CT) with other modern 3-D tomographic techniques. Each technique has its own niche for resolution and voxel matrix. Modified after Holzer & Cantoni (2011).

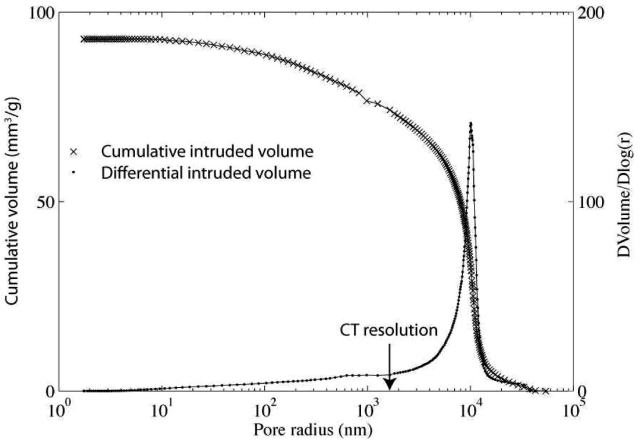

Figure 2. The curve with the cross marker represents the cumulative curve of the volume of intruded Hg. The curve with the dot markers displays the differential curves of the intruded Hg with respect to the apparent pore size distributions obtained for a subsample from a 10^3 cm^3 block of Berea sandstone.

porosity, helium density and mercury porosimetry were performed using a Helium Pycnometer 1330 (Micromeritics Instrument Corp., Belgium) and a Pascal 140 + 440 Mercury Porosimeter (Fig. 2; Thermo Electron Corporation, Germany), respectively. The resulting connected porosity is around 20 per cent. Permeability as provided by the company Berea Sandstone^{TM} Petroleum Cores is between 200 and 500 mD.

The mineral composition has been confirmed with petrographic microscopy and electron microprobe (Fig. 3). A hydrostatic compression test on Berea sandstone has shown that grain crushing and pore collapse occur at a critical pressure of P^* around 390 MPa (Wong & Baud 1999).

Crystallographic preferred orientation (CPO) of minerals may play a significant role in development of rock textures and consequent seismic anisotropy in reservoir rocks (Kendall et al. 2007). To investigate the potential CPO, we therefore measured the polycrystalline quartz texture of the Berea sandstone, using an XDS 2000 (Scintag, Inc., Cupertion, CA, USA) X-ray texture goniometer. A copper anode target was used to generate Cu-Kα X-rays, and the beam was operated at 40 kV and 45 mA. The sample holder and the sample itself were oscillating during the measurements to increase the area exposed to the X-ray beam and to obtain a better grain-counting statistic. Five incomplete pole figures were measured under the conditions listed in Table 1. The definition of terminology used in this table is given by Kocks *et al.* (1998). Pole figures were corrected for the background signal and the defocusing effect.

The MATLAB open-source software toolbox MTEX has been used to estimate the orientation distribution function (ODF; Bachmann *et al.* 2010). The five measured pole figures are used in the ODF calculation for quartz. The ODF is calculated using a finite Fourier series expansion and the de la Vallée–Poussin kernel (Hielscher *et al.* 2010). Pole figures were recalculated from the ODF and showed a good agreement with experimental pole figures. By using the MTEX extension for calculating physical properties (Mainprice *et al.* 2011), we computed the complete fourth-rank elastic stiffness tensor for the polycrystalline quartz aggregate. The single crystal elastic constants of quartz, used for calculation, are from McSkimin & Andreatch (1964). The elastic constants are reported in lower Reuss and upper Voigt bounds (Voigt 1928; Reuss 1929), as well as in the arithmetic Hill average (Hill 1952). These tensors have been used to calculate the *P*-wave velocity distribution in the aggregate (Fig. 4). The results show that for the Berea sandstone sample under analysis, the elastic tensor can be considered isotropic and exhibits a velocity anisotropy of less than 1 per cent. The results justify the use of the isotropic bulk and shear moduli for the complete aggregate in the numerical simulations.

3 DETERMINATION OF ULTRASONIC VELOCITY

Cylindrical samples of 25.4 mm in diameter were cored from a 10^3 cm^3 cube of homogeneous Berea sandstone for the acoustic measurements. These samples were cut to about 40 mm in length, and the end faces were ground flat and parallel with ± 5 μm precision. The cores were then oven dried at 100 °C for 1 week. The experiments took place in an oil-confined vessel at room temperature (25 °C). Changes in the length of the sample with pressure are considered insignificant. The acoustic velocities in the sample were measured over a range of confining pressures from an initial value of 230 MPa down to 5 MPa with the pulse transmission technique (Birch 1960; Christensen 1965; Toksöz *et al.* 1979) at 3 MHz. The results are given in Fig. 5.

The experimental data have been fitted with the function (Eberhart-Phillips *et al.* 1989)

$$V = a + kP_{\text{eff}} - b\text{e}^{(-dP_{\text{eff}})}, \quad (1)$$

where V is the velocity; a, k, b and d are coefficients whose values are found by a least-square fit and P_{eff} is the effective pressure. Table 2 shows the values of the coefficients of eq. (1), which approximates the non-linear increase of the velocity with effective pressures up to 50 MPa, followed by a linear increase for higher effective pressures.

4 X-RAY MICRO-CT OF BEREA SANDSTONE

Micro-CT scans were carried out on a Berea sandstone core sample of 6 mm diameter and 20 mm length. The core was subsampled

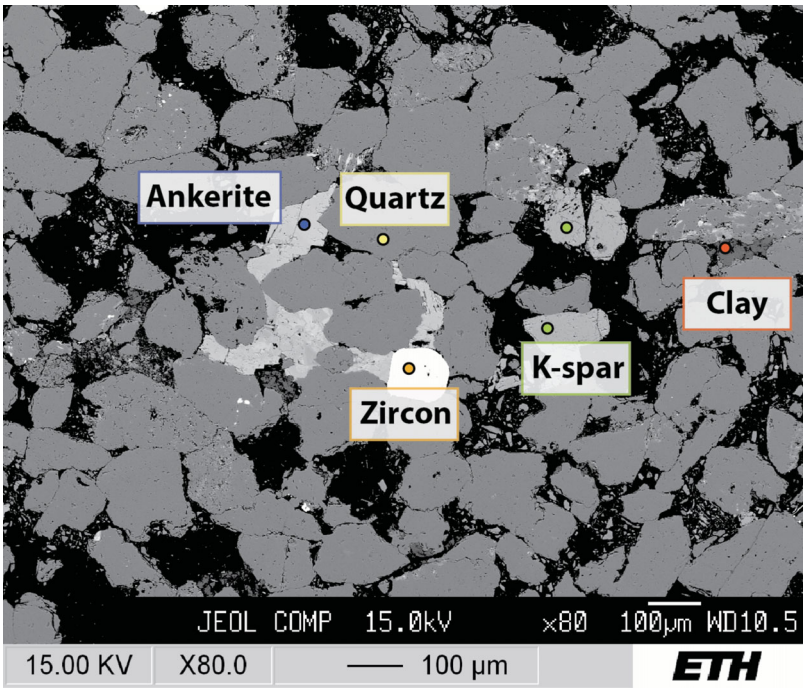

Figure 3. SEM images of the slice of Berea sandstone. Inclusions, cracks and mineral phases are clearly identified.

Table 1. Summary of pole figure measurement setup.

2θ Angle	hkil	Overlap weight (per cent)	PF range (max α)
20.82	10–10	100	60
26.65	10–11/01–11	70/30	65
39.49	10–12/01–12	17/83	70
50.15	11–21	100	75
59.96	21–31/12–31	53/47	80

from the same cube that was used for the extraction of the specimen used for ultrasonic measurements. Micro-CT images were measured with a SkyScan 1172 high-resolution desktop scanner (SkyScan NV, Kontich, Belgium), equipped with a 100 kV X-ray source and a 10 Megapixel CCD camera. The samples were scanned with an 81 kV tube voltage, a current of 109 μA and a 0.5 mm Al filter. The rotation increment was 0.31° for a full 360° rotation. Under these operating conditions, the resulting pixel size is 3.14 μm (resolution = 2 × pixel size = 6.28 μm). Attenuation of X-rays within the sample (considered at these energies) are related to the density of the material. The micro-CT scans therefore provide grey-scale images, which relate to the density of the analysed material.

Transmission images were reconstructed using SkyScan's NRecon cluster software v.1.6.1. Each reconstructed image slice is saved in 8-bit TIFF format. For each core, the complete data set consists of 1400 cross-sections.

4.1 Image segmentation

Image segmentation is the process of attributing a certain range of grey level to a particular mineral phase. Threshold segmentation was applied to the 8-bit grey-level TIFF images (raw data). The windows for the different mineral phases are chosen manually. After identifying the different mineral phases, the mineral edges are smoothed, and the areas inside the grains are filled using an automatic image filter. Three mineral phases have been chosen for segmentation: quartz, which is the main matrix, ankerite (ferric carbonate) and the empty pores. Other minerals, which amount to less than 3 volume per cent, have been segmented as quartz.

4.2 Segmentation of the unresolved grain-to-grain contact

We used the Binseparate function of the Avizo Fire software from VSG (Mégnac, France) to approximately define the grain-to-grain contacts. Binseparate is an implementation of an

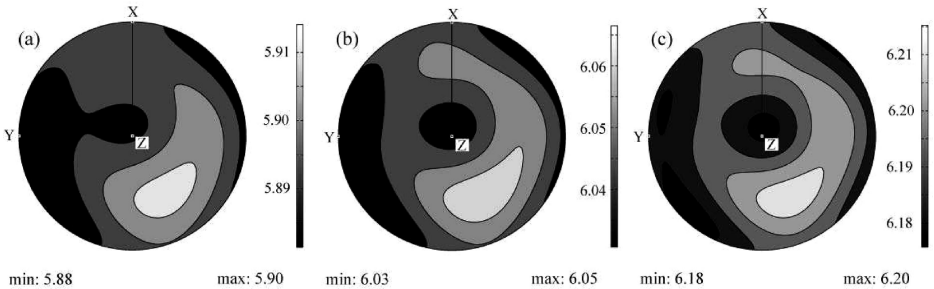

Figure 4. Lower hemisphere equal area projections of the calculated aggregate *P*-wave velocities, showing the (a) Reuss, (b) Hill and (c) Voigt estimates. The velocities were calculated with the MATLAB open source package MTEX (Hielscher *et al.* 2010; Mainprice *et al.* 2011).

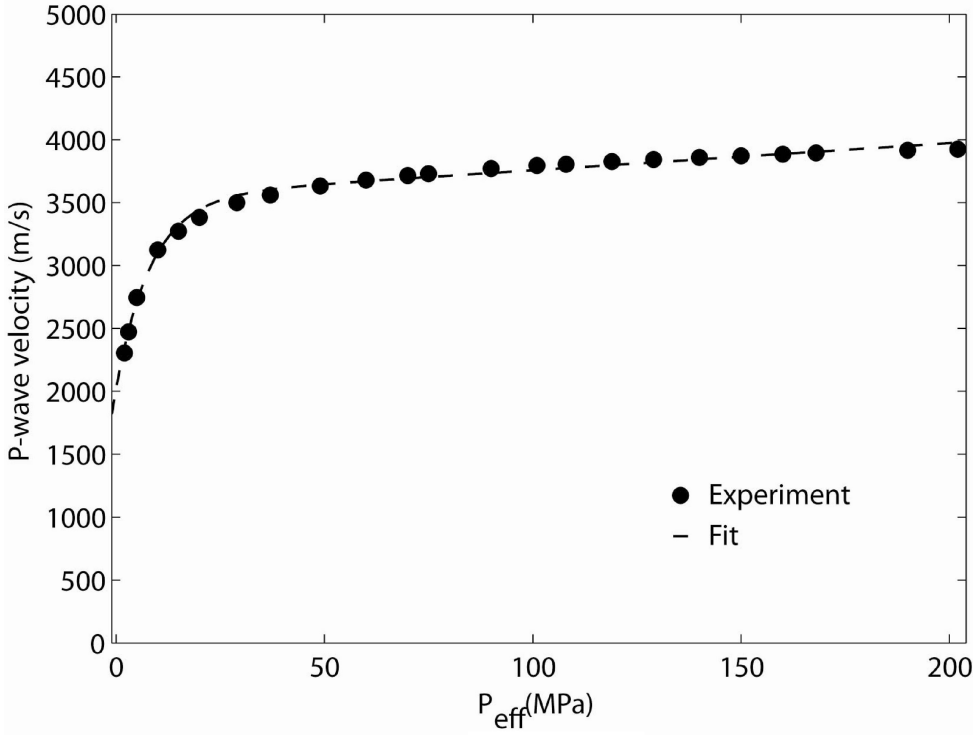

Figure 5. Experimental acoustic wave velocities in the Berea sandstone sample at 3 MHz as a function of the effective pressure. The dashed line represents the best fit using the relationship proposed by Eberhart-Phillips (1989).

Table 2. Velocity–pressure–moduli relationship.

Fitting parameters of: $a + k\,P_{\rm eff} - b \times \exp(-d\,P_{\rm eff})$	
a	3542
k	2.16
b	1526
d	0.119
$V_{\rm exp}\,(P_{\rm eff}) = s\,V_{\rm num}(M_{\rm contacts}, G_{\rm contacts})$	
s	0.7919
$P_{\rm eff} = c + w\,m_{g2g}$	
c (MPa)	0.9743
w (MPa)	200.86

algorithm described in the literature as the Grain Boundary Reconstruction (Henault *et al.* 1991; Arafin & Szpunar 2010). It is based on identifying watershed lines on the distance map of the grain space (e.g. Arns *et al.* 2007 and references therein). A detailed explanation can be found in the reference guide available for the Avizo Quantification module. The procedural steps are summarized as follows. After the threshold operation, as described in the previous section, the binary images are obtained. The binary images are then transformed onto grey-level images as a sum of successive erosions employing a distance transform. The result of the transform is a grey-level image, the distance map, that looks similar to the input images, with the difference that the grey-level intensities of points inside the grain regions are changed to show the distance to the closest boundary from each point. The resulting distance map is then inverted, and a contrast factor is added to the input images to calculate the regional minima. The regional minima of the reconstructed images are then used as particle markers for the watershed algorithm to determine the watershed lines. The watershed lines are subtracted from the initial images to obtain an approximation of the grain-to-grain contacts. The grain-to-grain contacts are then used subsequently on as a separate phase in the numerical experiments.

5 NUMERICAL ESTIMATION OF THE EFFECTIVE ELASTIC PROPERTIES

The micro-CT images obtained were post-processed to provide a 3-D digital model of the scanned rock for use in numerical simulations. The effective elastic properties can be determined using different numerical approaches. A review of the most important methods is given in Saenger (2008). In our study, the dynamic wave propagation method is used to determine the effective elastic properties (Saenger *et al.* 2004).

Elastic parameters in Table 3 were attributed to the identified grains during the segmentation. The mineral content has been analysed using X-ray diffraction (XRD) and electron scanning microprobe techniques. The grains are mainly quartz and ankerite. The latter is considered as calcite, as the elastic parameters for ankerite are not found in the literature. The pores are treated as vacuum. Then, the bulk effective medium parameters are estimated from the micro-CT images, as follows. A plane wave is applied to the boundary of one face of the 3-D rock model using a homogeneous buffer zone. Periodic boundary conditions are employed in the directions perpendicular to the chosen face. The wave propagation is based on an elastic finite-difference solver (Saenger *et al.* 2000). Because the wavelength (Table 3) used is much larger compared to the pore size, we can measure the effective velocities with this technique. Details of the numerical method are found in Saenger *et al.* (2011) and references therein.

In a first series of numerical experiments, the elastic properties of the grain-to-grain contacts are considered equivalent to those of quartz grains. This procedure is comparable to not applying the

Table 3. Modelling parameters and numerical estimated properties of the digitized sample.

Elastic moduli of crystals at room P & T, after Bass (1995)				
Property	*P*-wave modulus*	Bulk modulus	Shear modulus	Density
Symbol	M	K	G	ρ
Dimension	GPa	GPa	GPa	kg m^{-3}
Quartz	96.89	37.8	44.3	2648
Calcite	115.97	73.3	32	2712
Used parameters				
Sample size (gridpoints)			$400 \times 400 \times 400$	
Grid spacing			$\Delta h = 3.14\ \mu$m	
Sample thickness			$d = 400 \times 3.14\ \mu\text{m} = 1256\ \mu$m	
Porosity			21 per cent	
Dominant frequency of used wavelet			$f_{\text{dom}} = 1.59$ MHz	
Dominant wavelength @ 4000 m s^{-1}			$\lambda_{\text{dom}} = 0.0025\,\text{m} \approx 2\,d$	

*Calculated from $M = K + 4/3G$.

grain boundary reconstruction method, which allows identifying the grain-to-grain contacts. However, as shown by previous experiments and confirmed in this experiment (Fig. 5), the velocity increases exponentially with confining pressure. This behaviour is explainable with a spherical grain packing model (e.g. the Hertz–Mindlin model), where the theoretical effect of pressure change on the rock stiffness is predicted. Thus, it is reasonable to argue that the grain-to-grain contact moduli are highly dependent on the confining pressure. Therefore, additional numerical experiments have been performed with different values of the elastic moduli of the grain-to-grain contacts. These values range from 0 to the elastic moduli of quartz. The density is kept constant. Fig. 6 shows the two end-members of the 3-D digital rock used for the numerical simulations. Fig. 7 shows the results. By varying the value of the elastic moduli at grain-to-grain contacts, the calculated velocity displays a behaviour that is similar to the measurements obtained by the ultrasonic experiment under different confining pressures.

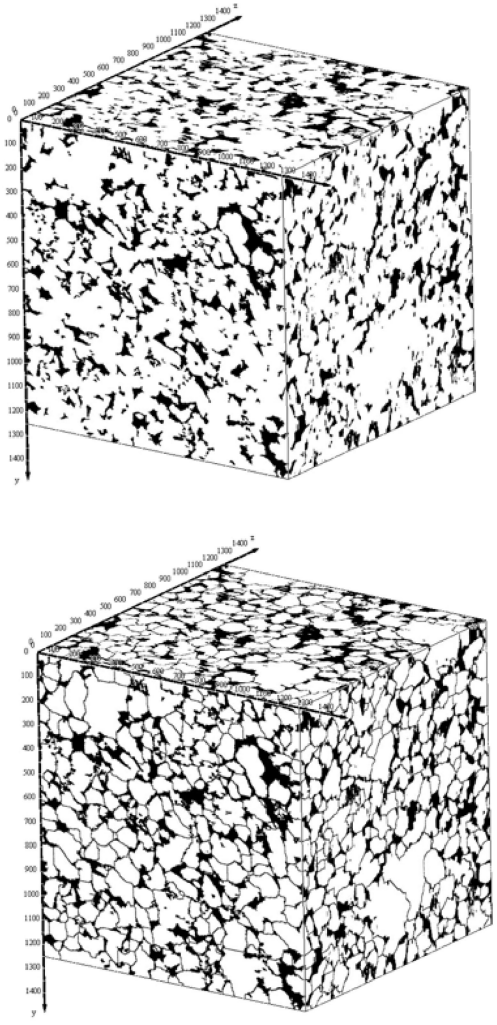

Figure 6. 3-D virtual rock cubes used for the calculation of the effective elastic properties. The upper cube represents the 100 per cent Quartz module end-member. The lower cube is the other end-member, when the grain-to-grain contact has a value of 0. The scales are in micrometres.

6 CALIBRATION

The laboratory velocity measurements at different confining pressures (Fig. 5) and the numerical results using different elastic parameters at the grain-to-grain contacts (Fig. 7) show a similar trend. Therefore, it can be assumed that the elastic moduli at the grain-to-grain contacts become higher with increasing confining pressure. However, the absolute values of laboratory (Fig. 5) and numerical experiments (Fig. 7) show substantial disagreement. As already reported in recent studies (Knackstedt *et al.* 2009; Zhang 2010), the calculated velocities from micro-CT images are higher than the laboratory observations. The effective elastic properties of a rock depend on the volume fractions of the various mineral phases and the geometric details of the constituents, such as the geometry and the grain-to-grain contacts (i.e. weaker mechanical parts). From scanning electron microscope images (SEM, Fig. 3) and the mercury porosimetry (Ritter & Drake 1945; Giesche 2006), it appears that a large portion of the pores and cracks are not resolved by the micro-CT imaging. Hence, all the weaker mechanical parts are not taken into consideration during the standard numerical simulation. As a consequence, the micro-CT imaging techniques cannot be used as a stand-alone tool to calculate the effective elastic properties of the rock. It is therefore necessary to calibrate the numerical results with the experimental data. We suggest a possible strategy of calibration for which the systematic higher velocities are corrected by

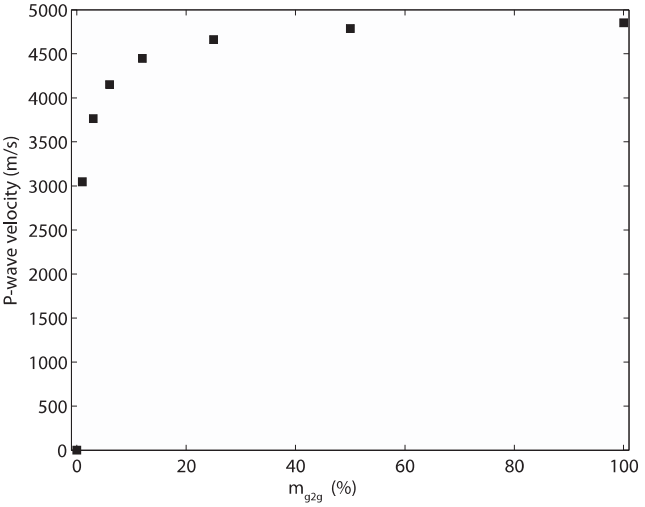

Figure 7. Computed compressional velocities as a function of the grain-to-grain contact moduli (M_{contacts}, G_{contacs}) that is expressed as a percentage of the quartz's moduli (m_{g2g}).

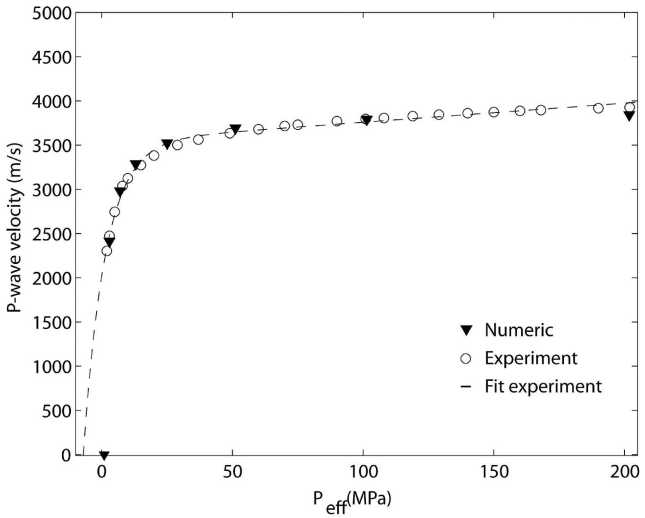

Figure 8. Acoustic velocities as a function of the effective pressure. The dashed line is the best fit of the experimental data. The triangles display the computed velocities calibrated with the experimental data.

multiplying the numerical velocity values (V_{num}) by a factor s:

$$V_{\text{exp}} = s\,V_{\text{num}}\,(M_{\text{contacts}}, G_{\text{contacts}})\,. \tag{2}$$

The second step is to attribute an effective pressure to the elastic moduli (M_{contacts} and G_{contacts}) at the grain-to-grain contacts. We suggest a linear relationship between the elastic moduli at the grain-to-grain contacts and the effective pressure:

$$P_{\text{eff}} = c + w m_{g2g}, \tag{3}$$

where $M_{\text{contacts}} = m_{g2g} M_{\text{Quartz}}$, $G_{\text{contacts}} = m_{g2g} G_{\text{Quartz}}$ and $m_{g2g} \in [0, 1]$. The values of the three parameters s, c and w are simultaneously obtained by the minimization of the unconstrained multivariable functions. Fig. 8 and Table 2 summarize the results.

7 DISCUSSION

Micro-CT imaging provides valuable information for calculating the effective elastic properties of rocks as it gives the geometric details of how the mineral phases are arranged. However, this technique still has limitations when combined with numerical simulations. The lack of resolution does not allow identification of cracks and pores in the micro- and nanometre ranges. Indeed, mercury porosimetry measurements (Fig. 2) indicate that a significant amount of the pore volume is below the resolution limit of micro-CT imaging. By visual inspection of the rock using SEM imaging that has higher resolution than micro-CT, we infer that two main features remain unresolved: the grain-to-grain contact zones and the small-scale cracks. Both significantly influence the effective mechanical properties. Several studies have demonstrated, based on different theoretical models (Mavko *et al*. 2009), the influence of the grain-to-grain contact on the effective compressibility of granular media. However, the grain-to-grain contacts can only partly be analysed visually and, because of noise in the images, they cannot be identified by a routine thresholding procedure, as described in Section 4.2. To solve this problem, an algorithm is required to geometrically separate grains that appear connected in micro-CT images.

In this study, we presented a method that uses laboratory measurements in conjunction with numerical simulations to overcome these restrictions. We suggest to include the grain-to-grain contacts as a separate segmented phase in the computation. We observed in the numerical results that varying linearly their moduli, M_{contacts} and G_{contacts}, yields a non-linear outcome of the effective elastic moduli. Similarly, in the laboratory experiments, a linear change in confining pressure produces a non-linear increase of the measured velocities.

Moreover, assigning an exact value for the elastic parameter to every grain is a challenging task. Several sources of error are introduced by attributing the moduli of a single crystal to the segmented grain. A single grain is considered homogeneous, whereas in reality it may contain microcracks and small inclusions (Passchier *et al.* 2005). Additionally, a crystal is often internally deformed with resultant lattice defects. Attributing the bulk modulus to only two phases (quartz and calcite) provides only a rough approximation. To resolve this problem, a scaling parameter, s, is introduced in the correction procedure (see eq. 2).

Lowering the elastic moduli of these mechanically weak zones allows to account for the pressure sensitivity of the grain boundary. To give physical meaning to the elastic moduli of the grain-to-grain contacts, we need to calibrate the moduli with the effective pressure. From the fitted results (Fig. 8), the calibration can then be used for subsurface pressure conditions from a few megapascals up to 200 MPa. The validity of the hereby presented approach does not consider the conditions close to room pressure as shown in Fig. 8. In addition, the range over which the approach is valid, in terms of confining pressure, has to be determined individually for each rock.

We assume that the coefficients s, c and w (eqs 2 and 3; Table 2) can be used for similar rocks (i.e. homogeneous sandstone), however a systematic approach has to be adopted in the future to test the uniqueness of the parameters on several types of rocks. Those variables depend also on the resolution of the CT-scan and the algorithm applied to segment the data. Therefore, it is necessary to calibrate the numerical simulation with experimental results each time CT images are used.

For similar or other rock types (e.g. same granular material but with different clay content between the grains), individual calibration is needed to estimate these coefficients. The parameters allow us to perform a coordinate mapping between the moduli of the grain-to-grain contact and the confining pressure. The parameters s, c and w are our proposed link between the numerical simulation and the experiment.

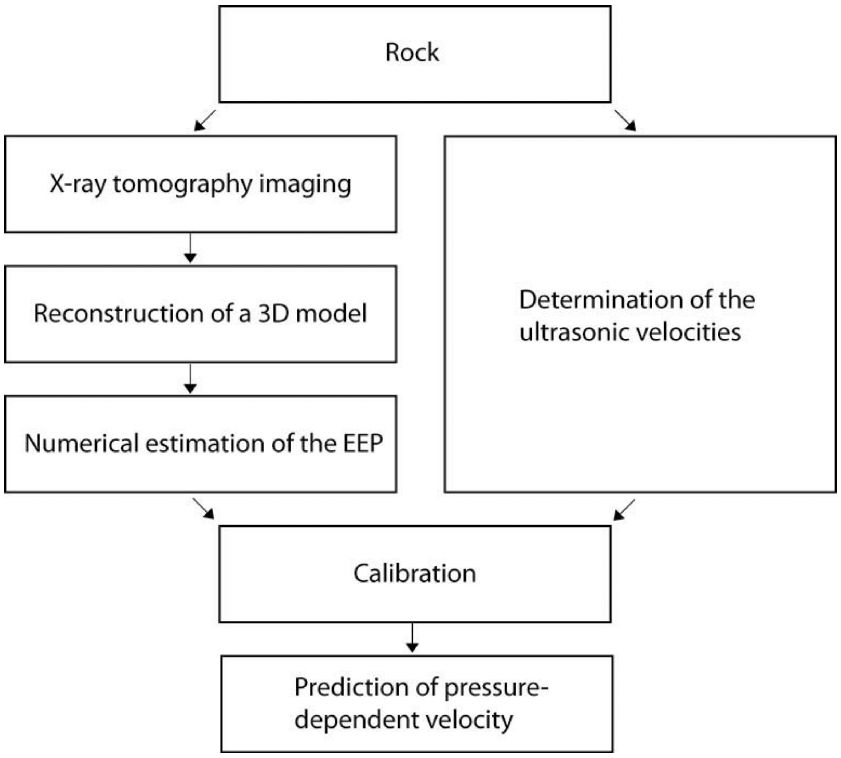

Figure 9. Workflow for a virtual rock laboratory that has to be calibrated with laboratory experiments.

8 CONCLUSIONS

In this paper, we present a workflow that integrates numerical simulations and laboratory experiments to obtain acoustic ultrasonic pressure-dependent velocity, summarized in Fig. 9. As part of the digital rock physics workflow, numerical and laboratory experiments must be combined for a better understanding of the physical properties of the rock. With modern imaging techniques, it remains difficult to resolve the microstructures (submicrometre) and image a representative volume at the same time, which is essential to understand the elastic properties of rocks.

We propose a calibration technique to numerically predict pressure-dependent velocities for a rock sample. The calibration provides a starting point for further dynamic simulations of wave propagation in solid media.

ACKNOWLEDGMENTS

Fruitful discussions with Marcel Frehner, Beatriz Quintal, Nima Riahi and Ronny Pini are acknowledged. This work was supported by the Swiss Commission for Technology and Innovation (CTI). EHS thanks the DFG (Deutsche Forschungsgemeinschaft) for their support through the Heisenberg scholarship (SA 996/1-2).

REFERENCES

Arafin, M.A. & Szpunar, J.A., 2010. Modeling of grain boundary character reconstruction and predicting intergranular fracture susceptibility of textured and random polycrystalline materials, *Comput. Math. Appl.,* **50**(2), 656–665, doi:10.1016/j.commatsci.2010.09.031.

Arns, C., Knackstedt, M.A., Pinczewski, M.V. & Lindquist, W.B., 2001. Accurate estimation of transport properties from microtomographic images, *Geophys. Res. Lett.,* **28**(17), 3361–3364, doi:10.1029/2001GL012987.

Arns, C., Knackstedt, M., Pinczewski, W. & Garboczi, E., 2002. Computation of linear elastic properties from microtomographic images. Methodology and agreement between theory and experiment, *Geophysics,* **67,** 1396–1405.

Arns, C., Madadi, M. & Sheppard, A., 2007. Linear elastic properties of granular rocks derived from Xray-CT images, in *International Exposition and Annual Meeting of the Society for the Exploration Geophysicists 2007,* Society of Exploration Geophysicists, Tulsa, OK.

Bachmann, F., Hielscher, R., Jupp, P.E., Pantleon, W., Schaeben, H. & Wegert, E., 2010. Inferential statistics of electron backscatter diffraction data from within individual crystalline grains, *J. appl. Cryst.,* **43,** 1338–1355, doi:10.1107/S002188981003027X.

Birch, F., 1960. The velocity of compressional waves in rocks to 10 kilobars. Part I, *J. geophys. Res.,* **65,** 4, doi:10.1029/JZ065i004p01083.

Christensen, N., 1965. Compressional wave velocities in metamorphic rocks at pressures to 10 kilobars, *J. geophys. Res.,* **70**(24), doi:10.1029/JZ070i024p06147.

Dvorkin, J., Armbruster, M., Baldwin, C. & Fang, Q., 2008. The future of rock physics: computational methods vs. lab testing, *First Break,* **26,** 63–68.

Eberhart-Phillips, D., Han, D. & Zoback, M., 1989. Empirical relationships among seismic velocity, effective pressure, porosity, and clay content in sandstone, *Geophysics,* **54**(1), 82–89.

Giesche, H., 2006. Mercury porosimetry: a general (practical) overview, *Part. Part. Syst. Char.,* **23**(1), 9–19, doi:10.1002/ppsc.200601009.s.

Harting, J., Chin, J., Venturoli, M. & Coveney, P.V., 2005. Large-scale lattice Boltzmann simulations of complex fluids: advances through the advent of computational Grids, *Phil. Trans. R. Soc. A.,* **363,** 1895–1915.

Henault, E., Coster, M. & Chermant, J., 1991, Grain-boundary reconstruction by automatic image-analysis on etch pits, *Mat. Res. Bull.,* **26**(7), 569–575.

Hielscher, R., Mainprice, D. & Schaeben, H., 2010. *Material Behavior: Texture and Anisotropy,* eds Freeden, W., Nashed, M.Z. & Sonar, T., Springer-Verlag, Berlin, Heidelberg, Germany.

Hill, R., 1952. The elastic behaviour of a crystalline aggregate, *Proc. Phys. Soc. Section A,* **65**(5), 349–354.

Holzer, L. & Cantoni, M., 2011. Review of FIB-tomography, in *Nanofabrication Using Focused Ion and Electron Beams: Principles and*

Applications, eds Utke, I., Moshkalev, S.A. & Russell, Ph., Oxford University Press, New York, NY. [ISBN 9780199734214]

Keehm, Y., Mukerji, T. & Nur, A., 2004. Permeability prediction from thin sections: 3D reconstruction and Lattice-Boltzmann flow simulation, *Geophys. Res. Lett.,* **31**(4), doi:10.1029/2003GL018761.

Kendall, J.-M. *et al*., 2007, Seismic anisotropy as an indicator of reservoir quality in siliciclastic rocks, *Geol. Soc. Lond. Spec. Publ.,* **292,** 123–136.

Knackstedt, M. & Arns, C., 2005. Velocity–porosity relationships: predictive velocity model for cemented sands composed of multiple mineral phases, *Geophys. Prospect,* **53,** 349–372, doi:10.1111/j.1365-2478.2005.00479.x.

Knackstedt, M.A., Latham, S., Madadi, M., Sheppard, A. & Varslot, T., 2009. Digital rock physics: 3D imaging of core material and correlations to acoustic and flow properties, *Leading Edge,* **28**(1), 1–5.

Kocks, U.F., Tome, C.N. & Wenk, H.-R., 1998. *Texture and Anisotropy,* Cambridge University Press, Cambridge.

Leurer, K.C. & Dvorkin, J., 2006. Viscoelasticity of precompacted unconsolidated sand with viscous cement, *Geophysics,* **71**(2), doi:10.1190/1.2187795.

Madadi, M., Jones, A.C., Arns, C.H. & Knackstedt, M.A., 2009. 3D imaging and simulation of elastic properties of porous materials, *Comput. Sci. Eng.,* **11**(4), 65–73.

Mainprice, D., Hielscher, R & Schaeben, H., 2011. Calculating anisotropic physical properties from texture data using the MTEX open source package, *Geol. Soc. Lond. Spec. Publ.,* **360,** 175–192.

Malinouskaya, I. & Mourzenko, V., 2008. Wave propagation through saturated porous media, *Phys. Rev. E,* **77**.

Mavko, G., Mukerji, T. & Dvorkin, J., 2009. *The Rock Physics Handbook,* Cambridge University Press, Cambridge.

McSkimin, H. & Andreatch, P., 1964. Elastic moduli of quartz versus hydrostatic pressure at 25.0 C and -195.8 C, *J. appl. Phys.,* **35**(7), 2161–2165.

Øren, P.-E.; Bakke, S. & Held, R., 2007. Direct pore-scale computation of material and transport properties for North Sea reservoir rocks, *Water Resour. Res.,* **43,** doi:10.1029/2006WR005754.

Passchier, C.W., Rudolph, A. & Trouw, J., 2005. *Microtectonics,* Springer-Verlag, Berlin, Heidelberg, Germany.

Reuss, A., 1929. Berechnung der Fliessgrenze von Mischkristallen auf Grund der Plastizität für Einkristalle, *Zeitschrift für Angewandte Mathematik und Mechanik,* **9**(1), 49–58.

Ritter, H.L. & Drake, L.C., 1945. Pore-size distribution in porous materials: pressure porosimeter and determination of complete macropore-size distributions, *Ind. Eng. Chem.,* **17**(12), 782–786.

Saenger, E.H., 2008. Numerical methods to determine effective elastic properties, *Int. J. Eng. Sci.,* **46**(6), 598–605, doi:10.1016/j.ijengsci.2008.01.005.

Saenger, E.H., Gold, N. & Shapiro, S.A., 2000. Modeling the propagation of elastic waves using a modified finite-difference grid, *Wave Motion,* 77–92.

Saenger, E.H., Kruger, O. & Shapiro, S., 2004. Numerical considerations of fluid effects on wave propagation: influence of the tortuosity, *Geophys. Res. Lett.,* **31,** doi:10.1029/2004GL020970.

Saenger, E.H., Enzmann, F., Keehm, Y. & Steeb, H., 2011. Digital rock physics: effect of fluid viscosity on effective elastic properties, *J. appl. Geophys.,* **24,** 236–241.

Sakellariou, A. *et al*., 2007. Developing a virtual materials laboratory, *Materials Today,* **10**(12), 44–51, doi:10.1016/S1369-7021(07)70307-3.

Toksöz, M., Johnston, D. & Timur, A., 1979. Attenuation of seismic-waves in dry and saturated rocks .1. Laboratory measurements, *Geophysics,* **44**(4), 681–690.

Voigt, W., 1928. *Lehrbuch der Kristallphysik,* Teubner, Leipzig, Germany.

Wong, T.F. & Baud, P., 1999. Mechanical compaction of porous sandstone, *Oil Gas Sci. Technol. Rev. IFP,* **54**(6), 715–727.

Zhang, Y., 2010. Modeling of the effects of wave-induced fluid motion on seismic velocity and attenuation in porous rocks, *PhD thesis*. Massachusetts Institute of Technology, Cambridge, MA.